

# NON-EQUILIBRIUM IONIZATION IN THE MULTIPHASE CIRCUMGALACTIC MEDIUM—IMPACT ON QUASAR ABSORPTION-LINE ANALYSES

SUYASH KUMAR<sup>1</sup>  AND HSIAO-WEN CHEN<sup>1,2</sup> 

<sup>1</sup>Department of Astronomy and Astrophysics, The University of Chicago, Chicago, IL 60637, USA and

<sup>2</sup>Kavli Institute for Cosmological Physics, The University of Chicago, Chicago, IL 60637, USA

Version January 24, 2025

## Abstract

This paper presents an updated framework for studying the ionizing conditions and elemental abundances of photoionized, metal-enriched quasar absorption systems. The standard assumption of ionization equilibrium invoked in absorption line analyses requires gas to cool on longer timescales than ionic recombination ( $t_{\text{cool}} \gg t_{\text{rec}}$ ). However, this assumption may not be valid at high metallicities due to enhanced cooling losses. This work presents a suite of time-dependent photoionization (TDP) models that self-consistently solve for the ionization state of rapidly cooling gas irradiated by the extragalactic ultraviolet background (UVB). The updated framework explores various revised UVBs from recent studies, a range of initial temperatures, and different elemental abundance patterns to quantify the effects of TDP on the observed ion fractions. A metal-enriched ( $[\alpha/\text{H}] = 0.6^{+0.2}_{-0.1}$ ) C IV absorption system at  $z \sim 1$  previously studied using photoionization equilibrium (PIE) models is re-examined under the TDP framework. The main findings are as follows: (1) varying prescriptions for the underlying UVB or adopting initial temperatures  $T_0 \lesssim 10^6$  K change TDP ion fractions by up to a factor of three, but the adopted relative elemental abundance pattern affects ion fractions by at most 40%; (2) the inferred gas densities are consistent between PIE and TDP, but under TDP solar metallicity cannot be ruled out at more than  $2\text{-}\sigma$  significance and a modest non-solar  $[\text{C}/\alpha] \approx 0.2$  is needed to explain the observed relative ion abundances. Extending the TDP analyses to a larger sample of super-solar absorption components with high signal-to-noise absorption spectra is needed to quantify the fraction of metal absorbers originating in rapid cooling gas.

*Subject headings:* Extragalactic astrophysics – circumgalactic medium – quasar absorption spectroscopy – ionization modeling

## 1. INTRODUCTION

Quasar absorption line spectroscopy provides a powerful tool for probing tenuous gas reservoirs in galaxies. Studies using this technique have led to detections of gaseous clouds out to virial radii and beyond (see e.g., [Chen et al. 2001, 2010](#); [Borthakur et al. 2013](#); [Liang & Chen 2014](#); [Huang et al. 2016, 2021](#); [Burchett et al. 2016, 2019](#)), which constitute the circumgalactic medium (CGM). Absorption systems have been found to host low-, intermediate-, and high-ionization species, sometimes simultaneously (see e.g., [Chen & Prochaska 2000](#); [Meiring et al. 2013](#); [Burchett et al. 2015](#); [Nevalainen et al. 2017](#); [Zahedy et al. 2019, 2021](#); [Sankar et al. 2020](#); [Haislmaier et al. 2021](#); [Cooper et al. 2021](#); [Qu et al. 2023, 2024](#); [Sameer et al. 2024](#); [Kumar et al. 2024](#)). This indicates a vast range of thermodynamic properties in the CGM; specifically, the CGM exists in the cool ( $T \approx 10^{4-4.5}$  K), warm-hot ( $T \approx 10^{4.5-5.5}$  K), and hot phase ( $T \gtrsim 10^{5.5}$  K). These phases also differ in their baryon and metal budget (see e.g., [Werk et al. 2014](#); [Peebles et al. 2014](#)), besides their thermodynamic properties and spatial extent.

Thermodynamic properties and elemental abundances cannot directly be inferred for absorption arising from ionized gas. Therefore, ionization models are necessary to infer gas

properties from absorption line measurements. To do so, measured relative abundances of ionic species are compared with expectations from ionization models across a grid of gas properties. Available choices of ionization models vary in their incorporation of ionizing radiation. For instance, because collisional interactions are subdued at lower temperatures, the cool and warm-hot CGM are considered to be photoionized by the extragalactic ultraviolet background (see e.g., [Bergeron & Stasińska 1986](#); [Rauch et al. 1997](#); [Keeney et al. 2013, 2017](#); [Werk et al. 2014](#); [Crighton et al. 2015](#); [Zahedy et al. 2019](#); [Sankar et al. 2020](#); [Zahedy et al. 2019, 2021](#); [Cooper et al. 2021](#); [Haislmaier et al. 2021](#); [Qu et al. 2022, 2023](#); [Sameer et al. 2024](#)). In contrast, hot gas is assumed to be collisionally ionized because of having a higher temperature (see e.g., [Tripp et al. 2011](#); [Meiring et al. 2013](#); [Hussain et al. 2015](#); [Pachat et al. 2017](#); [Nevalainen et al. 2017](#); [Rosenwasser et al. 2018](#)).

Both photo- and collisional ionization models typically assume equilibrium conditions. Under this assumption, the gas must cool slowly relative to ionic recombination timescales, so a steady state can be assumed. However, at high metallicities, cooling losses are enhanced through collisional, free-bound, and free-free interactions; the cooling time becomes shorter than ionic recombination, resulting in a departure from ionization equilibrium (see e.g., [Gnat & Sternberg 2007](#)). In such cases, a steady state cannot be assumed, and equations of ionization balance must be solved simultaneously with energy

conservation to compute time-dependent ion fractions.

Studies of hot gas have considered both collisional equilibrium and non-equilibrium models (see e.g., [Tripp et al. 2011](#); [Meiring et al. 2013](#); [Hussain et al. 2015](#); [Pachat et al. 2017](#); [Nevalainen et al. 2017](#); [Rosenwasser et al. 2018](#)). The cool phase has been established to be in photoionization equilibrium (see e.g., [Zahedy et al. 2019](#); [Qu et al. 2022](#); [Sameer et al. 2021](#); [Zahedy et al. 2021](#); [Cooper et al. 2021](#)), justified by the inferred sub-solar metallicities which are not sufficient to cause rapid cooling. Photoionization equilibrium models have also been used for the warm-hot phase (see e.g., [Sankar et al. 2020](#); [Kumar et al. 2024](#)), but the inferred metallicities at a solar level or above pose a challenge because of enhanced cooling losses expected at these enrichment levels. Additionally, [Kumar et al. \(2024\)](#) find a discrepancy between the ionization equilibrium model temperature and line width temperature in the C IV-selected warm-hot CGM. These caveats motivate the usage of non-equilibrium photoionization models for metal-enriched warm-hot gas.

Non-equilibrium (or time-dependent) photoionization by the extragalactic ultraviolet background (UVB) has been discussed by [Oppenheimer & Schaye \(2013\)](#) and [Gnat \(2017\)](#). Both studies demonstrate that the ionization state of a rapidly cooling gas differs from the equilibrium scenario. In addition, photoionization modifies the initial overabundance of high-ionization species arising from recombination lags, further amplifying the discrepant ionization balance. An important distinction between photoionization equilibrium and non-equilibrium is the added dependence of ion ratios on gas metallicity and temperature. Therefore, systematic differences in inferred gas properties may exist using photoionization equilibrium versus non-equilibrium models. However, before comparing non-equilibrium models with absorption line measurements, some systematics regarding this class of models are worth highlighting.

The primary ingredient for photoionization models is the assumed ionizing radiation background. The CGM, being spatially extended, remains largely unaffected by ionizing radiation arising locally within the galaxy halo (e.g., [Qu et al. 2023](#)). Instead, the CGM is ionized by the UVB, which has contributions from quasars and star-forming galaxies. There are various prescriptions available for the ionizing background (see e.g., [Haardt & Madau 2001, 2012](#); [Khaire & Srianand 2019](#); [Faucher-Giguère 2020](#)); these prescriptions differ in their amplitude and slope, influencing ion fractions in photoionized gas (see e.g., [Chen et al. 2017](#); [Zahedy et al. 2019](#); [Lehner et al. 2022](#)). Non-equilibrium models from [Oppenheimer & Schaye \(2013\)](#) and [Gnat \(2017\)](#) use UVB prescriptions from [Haardt & Madau \(2001\)](#) and [Haardt & Madau \(2012, HM12\)](#). In the past decade, extensive efforts have been directed towards revising UVB models to incorporate updated statistics of Ly $\alpha$  forest absorbers and improved constraints on AGN luminosity functions/x-ray extragalactic background. As such, recent prescriptions from ([Khaire & Srianand 2019, KS19](#)) and ([Faucher-Giguère 2020, FG20](#)) have not been incorporated into time-dependent photoionization models. In addition to the ionizing background, the adopted initial temperature from which the gas is assumed to cool is another important ingredient in non-equilibrium ionization models. This is because the initial temperature sets the starting ionic composition of the gas, which affects the subsequent ionization state of the gas through time-dependent cooling. Finally, the adopted elemental abundance pattern sets the relative cooling losses from individual elements (see e.g., [Gnat & Ferland](#)

[2012](#)), which are coupled to the ion fractions. It is crucial to explore the variance in non-equilibrium ion fractions resulting from uncertainties in these three model assumptions.

The additional dependence of ion fractions on gas temperature and metallicity under non-equilibrium photoionization is important to address when comparing model predictions with absorption line measurements. In absorption line systems with ions of sufficiently different mass, the line broadening can be decomposed into thermal and non-thermal contributions (see e.g., [Rauch et al. 1996](#); [Rudie et al. 2019](#); [Zahedy et al. 2019](#); [Qu et al. 2022](#); [Kumar et al. 2024](#)). In situations where the gas temperature can be determined using the observed absorption line widths, the assumed temperature in the photoionization calculations can be fixed to the line width temperature to reduce degeneracies between different gas properties during ionization modeling (see e.g., [Sameer et al. 2024](#)).

This work presents a new suite of time-dependent photoionization models with flexible choices for the adopted radiation background, initial temperature, and elemental abundance pattern. The impact of varying model assumptions on non-equilibrium fractions is explored. Following this, a grid of time-dependent photoionization models is compared with absorption-line measurements of the highest metallicity C IV absorber from [Kumar et al. \(2024\)](#). Finally, gas properties (density, metallicity, and relative abundances) inferred using non-equilibrium models are compared with those from equilibrium models.

This paper is organized as follows. In § 2, the construction of ionization models is presented. In § 3, the impact of varying individual model assumptions on non-equilibrium fractions is discussed, followed by comparing model predictions with absorption line measurements. In § 4, a summary of the key findings from the study is presented alongside caveats.

## 2. METHOD

This section presents the details of building ionization models for examining absorption line measurements. Specifically in § 2.1, key ingredients for photoionization equilibrium models and caveats of using such models are highlighted, and in § 2.2, time-dependent photoionization as an alternative to equilibrium models for examining metal-enriched gas is presented.

### 2.1. Photoionization equilibrium

Ionization analyses of cool and warm-hot diffuse gases typically assume photo-ionization equilibrium (PIE). The gas is irradiated by the extragalactic UVB. Some available UVB prescriptions are shown in Figure 1. The ionization state of gas in PIE is set by a balance between photoionization and ionic recombination. A useful quantity for characterizing PIE fractions is the ionization parameter  $U \equiv n_\gamma/n_H$ , which quantifies the ratio of ionizing photons to baryons. PIE fractions primarily depend on the ionization parameter and are only weakly dependent on metallicity and temperature. Therefore, measured ion ratios from absorption line systems can be compared with expectations from PIE to constrain the ionization parameter robustly. Under the assumption of a fixed radiation field, a constraint on the ionization parameter translates to a measure of the gas density.

A test for the validity of PIE is comparing the ionization model temperature with the line width temperature. PIE assumes thermal equilibrium, with the gas temperature set by a balance between radiative cooling from collisional processes and photoheating by the UVB. Figure 2 depicts the cooling

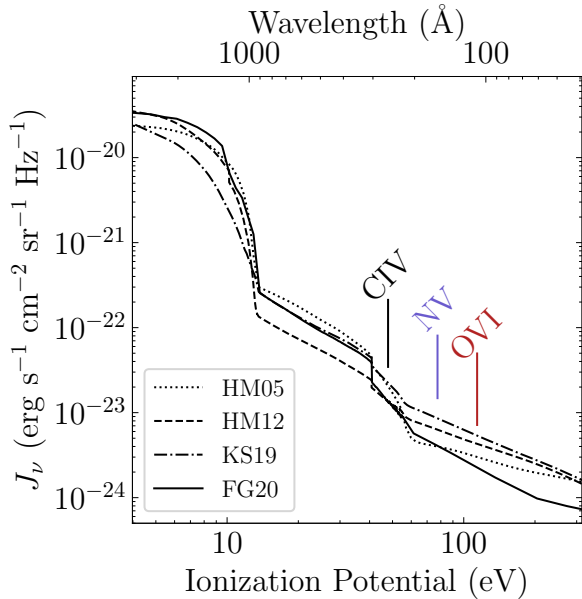


FIG. 1.— Differences in the expected UVB at  $z = 1$  based on commonly adopted prescriptions. HM05 refers to an updated version from [Haardt & Madau \(2001\)](#) made available in CLOUDY, while HM12, KS19, and FG20 refer to [Haardt & Madau \(2012\)](#), [Khairi & Srianand \(2019\)](#), and [Faucher-Giguère \(2020\)](#), respectively. The ionization potentials for C IV, N V, and O VI—key tracers of warm-hot gas—are also marked.

and heating rates for gas at solar and sub-solar metallicities, assuming a fiducial gas density of  $n_{\text{H}} = 10^{-3} \text{ cm}^{-3}$ . The equilibrium temperature depends on the gas metallicity, with higher enrichment levels leading to lower temperatures. The equilibrium temperature corresponding to the best-fit ionization model can be compared with the temperature estimated by comparing the absorption line widths from ionic species with sufficiently different masses (see e.g., [Qu et al. 2022](#); [Kumar et al. 2024](#)).

A recent investigation of C IV absorbers at  $z \sim 1$  from [Kumar et al. \(2024, hereafter Paper I\)](#) pursued ionization modeling of 12 kinematically resolved absorption components. The equilibrium temperature  $T_{\text{PIE}}$  for each component was determined based on the best-fit gas density and metallicity. The kinematic temperature was obtained using the best fit line widths of the H I and C IV components that were found to occupy the same phase during ionization modeling. The line width temperature was found to exceed the PIE temperature at a  $>3\text{-}\sigma$  level for the C IV-bearing gas phase at  $z_{\text{abs}} = 1.26, c3$  (see §3.2). Incidentally, this phase also had the highest inferred metallicity in the sample, with  $[\alpha/\text{H}] \approx 0.6$ . The cooling time for this system is 7.5 Myr, shorter than the C V  $\rightarrow$  C IV recombination time of 12 Myr. The mismatched cooling and recombination time scales indicate that the gas is likely out of equilibrium in this metal-enriched system.

In principle, the temperature discrepancy can be addressed by fixing the gas temperature adopted for PIE calculations to be consistent with the observed thermal broadening (see e.g., [Hussain et al. 2015](#); [Pachat et al. 2017](#)). Physically, such a model assumes the presence of an unknown heating source, elevating the equilibrium temperature compared to UVB-only heating (Figure 3). In the measured temperature

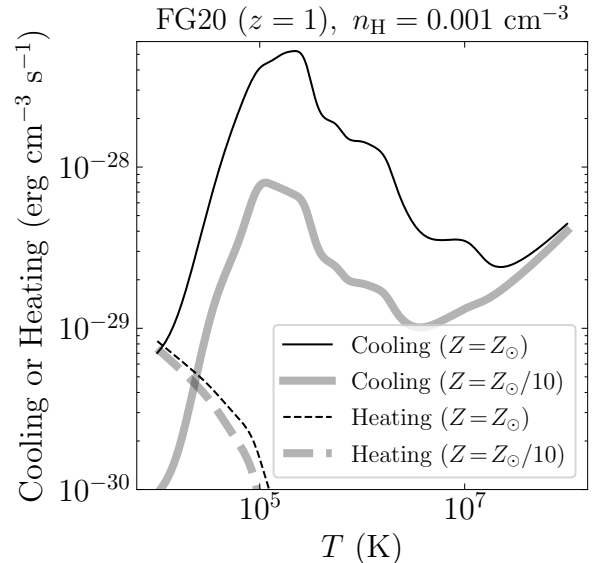


FIG. 2.— The expected cooling and heating under photoionization equilibrium (see also [Wiersma et al. 2009](#)). A gas density of  $n_{\text{H}} = 0.001 \text{ cm}^{-3}$  is assumed and the UV background from [Faucher-Giguère \(2020\)](#) is adopted. Models for solar and one-tenth-solar gas metallicities are depicted using thin and thick lines, respectively.

range  $T \lesssim 2.5 \times 10^4 \text{ K}$ , PIE ion fractions show only modest variations (see e.g., [Gnat 2017](#), also Figure 4). Therefore, the gas properties inferred from this modified calculation would be consistent with the original PIE results presented in Paper I (summarized in §3.2). Although this approach may resolve the tension between the PIE temperature and the observed line broadening, caveats remain in identifying a suitable astrophysical source that can provide heating without modifying the spectral shape of the ionizing radiation (see §4). As discussed in the next section and in §3.2, time-dependent photoionization (TDP) offers an alternative framework for reproducing absorption line measurements by modeling rapid gas cooling at high metallicities.

## 2.2. Time-dependent photoionization

Chemically enriched gas clouds are expected to experience enhanced cooling losses through collisional, free-bound, and free-free interactions. In ionization equilibrium, because the gas cools slowly, ion fractions can be assumed to be in a steady state at all times ( $dx_{\text{ion}}/dt = 0$ ). However, a steady state cannot be assumed if cooling is rapid. In such cases, equations of ionization balance must be solved simultaneously with energy conservation to specify the ionization state of the gas over time. At high metallicities ( $Z \gtrsim Z_{\odot}$ ), when cooling is enhanced, the gas becomes "overionized" relative to the equilibrium scenario because of an overabundance of high ions caused by recombination lag (see e.g., [Gnat & Sternberg 2007](#)).

Non-equilibrium collisional ionization models from [Gnat & Sternberg \(2007\)](#) have been compared with absorption line systems arising from hot gas (see e.g., [Tripp et al. 2011](#); [Meiring et al. 2013](#); [Hussain et al. 2015](#); [Nevalainen et al. 2017](#); [Rosenwasser et al. 2018](#)). However, photoionization from the extragalactic UVB cannot be neglected at temperatures relevant for some high-ionization species. The inclusion of a radiation background in time-dependent calculations modifies

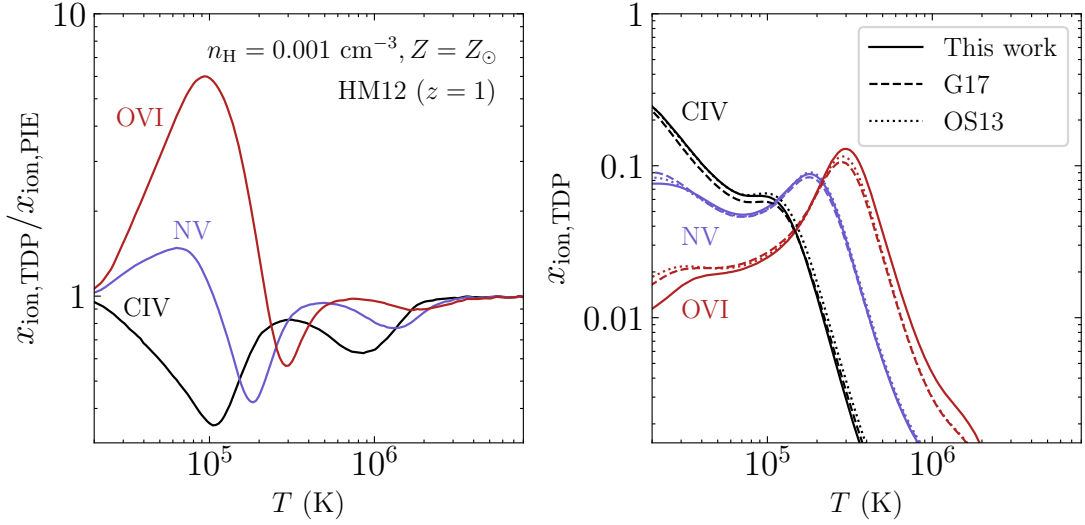


FIG. 3.— Impact of time-dependent photoionization in the predicted ion fractions based on the framework presented in this paper and those from previous studies. The *left* panel shows differences in the predicted ion fractions  $x_{\text{ion}}$  between TDP and PIE models for C IV, N V, and O VI. Different species are indicated with different colors. Gas density and metallicity are kept fixed at  $n_{\text{H}} = 0.001 \text{ cm}^{-3}$  and  $Z = Z_{\odot}$  respectively. The ionizing radiation is assumed to be from HM12 to facilitate comparisons with literature. The *right* panel contrasts the predicted non-equilibrium  $x_{\text{ion}}$  from this work with those from [Gnat \(2017\)](#) and [Oppenheimer & Schaye \(2013\)](#). The expected TDP  $x_{\text{ion}}$  are largely consistent between these studies with differences attributed to updated atomic data.

the ionization state of gas through photoionization and photoheating (see e.g., [Oppenheimer & Schaye 2013](#); [Gnat 2017](#)). This is illustrated in the left panel of Figure 3, which shows the differences in the predicted ion fractions  $x_{\text{ion}}$  between PIE and TDP models for three commonly adopted tracers of warm-hot ionized gas, C IV, N V, and O VI, in QSO absorption-line studies.

Note that the PIE fractions vary with gas density but do not depend on metallicity, while the predicted TDP fractions have a simultaneous density and metallicity dependence. The discrepancy between TDP and PIE is therefore metallicity dependent. For a solar metallicity gas of density  $n_{\text{H}} = 0.001 \text{ cm}^{-3}$ , O VI can be overabundant by an order of magnitude at  $T \approx 10^5$  K. N V behaves similarly as O VI, but C IV is underabundant relative to PIE at this density because of an overabundance in C V at these cooler temperatures.

The photoionization models presented in this paper are calculated using an updated CLOUDY photoionization code (version 22.01, see [Ferland et al. 2017](#); [Chatzikos et al. 2023](#)). In particular, the hazy1 documentation provides a non-equilibrium cooling calculation script for modeling the radiative time-dependent cooling in a plane parallel gas slab without any ionizing radiation, following [Gnat & Sternberg \(2007\)](#). The default script is modified to include ionizing radiation from a UVB<sup>1</sup>. The cooling is assumed to be isochoric, and the calculations stop at thermal equilibrium or  $10^4$  K, whichever condition is achieved first. The gas is also assumed to be optically thin for these calculations.

Since the publication of previous TDP calculations, the atomic data has been updated. Specifically, the cooling efficiencies have been updated across different versions of CLOUDY, which affects non-equilibrium fractions by extension because of the coupling between cooling losses and ionization state. Non-equilibrium calculations in Figure 3 were per-

formed assuming the HM12 UVB and an initial temperature of  $T_0 = 10^8$  K to enable direct comparisons with [Gnat \(2017\)](#) and [Oppenheimer & Schaye \(2013\)](#). The right panel of Figure 3 shows that all three studies produce consistent  $x_{\text{ion}}$  under TDP with differences of less than a factor of two at  $T \lesssim 3 \times 10^4$  K. This is an important caveat to consider when comparing the latest TDP calculations with those in the literature.

In addition to atomic data, the extragalactic ionizing background has also been updated since previous TDP calculations were performed (Figure 1). Therefore, there is a need to perform TDP calculations using updated KS19 and FG20 UVB prescriptions. The left panel of Figure 4 shows the expected PIE fractions under three different UVB prescriptions, which can differ by a factor of several at  $T \lesssim 10^5$  K (see also [Chen et al. 2017](#); [Zahedy et al. 2019](#)). The differences in the predicted  $x_{\text{ion}}$  of these intermediate- to high-ionization species can be attributed to the spectral slope of the adopted UVB with a softer spectrum (e.g., FG20) and lower intensities at high frequencies that led to lower high-ion fractions. The discrepancy due to different adopted UVB models continues to affect the predicted TDP fractions, as shown in the right panel of Figure 4.

It was shown in Paper I that under the PIE assumption C IV absorption preferentially arise in diffuse gas of  $\log(n_{\text{H}}/\text{cm}^{-3}) \approx -3.5$  and high metallicities of  $[\alpha/\text{H}] \gtrsim -1$ . TDP fractions in this density-metallicity range can depart significantly from the equilibrium values. Because gas properties are inferred by comparing measured ion ratios with ionization model predictions, the results of such a comparison can differ between TDP and PIE.

This work will re-examine the highest metallicity C IV component from Paper I under a TDP framework. To do so, the TDP calculations highlighted before are performed for a grid of gas densities and metallicities. An ionization analysis comparing absorption line measurements with TDP models reveals how inferred gas properties change compared to a PIE analy-

<sup>1</sup> See [this ReadMe](#) for a tutorial on building a suite of TDP models.

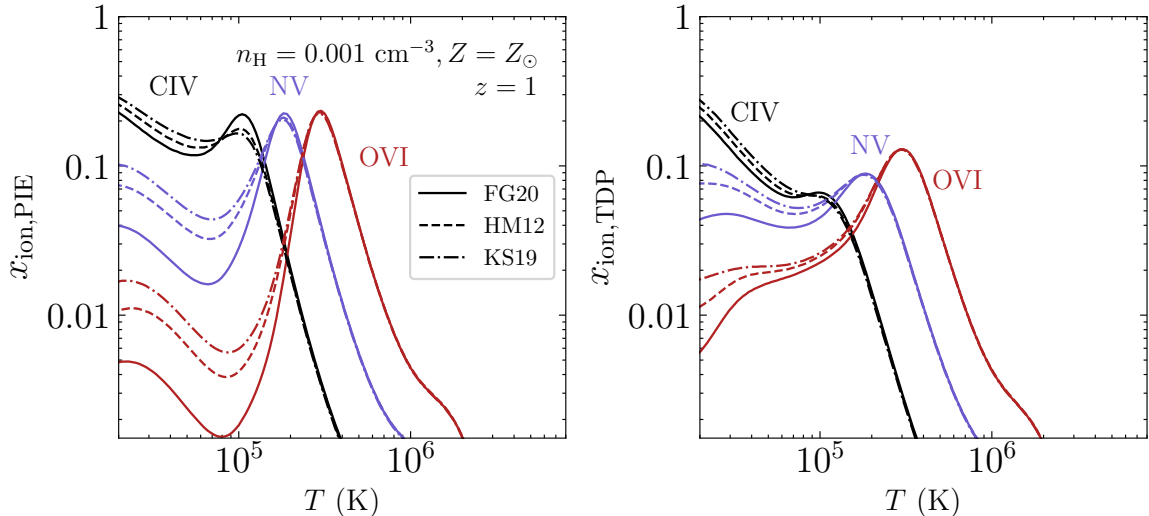


FIG. 4.— Impact of different UVBs in the predicted ion fractions under PIE and TDP conditions. The *left* panel shows expected PIE ion fractions  $x_{\text{ion}}$  for C IV, N V, and O VI assuming different UVB prescriptions. A fixed gas density of  $n_{\text{H}} = 0.001 \text{ cm}^{-3}$  and metallicity of  $Z = Z_{\odot}$  are assumed for all calculations. The *right* panel repeats the exercise from the left panel but for TDP conditions.

sis. Note that for the systems of interest, the gas temperature is well-constrained from available absorption line widths of elements with sufficiently different masses. In fact, the temperature estimate using absorption line widths was found to be discrepant with the PIE model temperature. Therefore, when comparing TDP models with absorption line measurements, the model temperature is fixed to the line width temperature. A direct implication of this approach is that the gas is in a transient phase, still undergoing cooling and not yet having reached thermal equilibrium. This is distinct from the steady-state PIE solution discussed in the previous section which requires additional heating from some unspecified source (see § 4 for further discussion).

### 3. ANALYSIS

Time-dependent photoionization models provide a self-consistent framework for examining metal-enriched absorption systems. However, the underlying assumptions for TDP models can have a notable effect on the expected ion fractions. Here the effect of varying individual ingredients in the TDP models is evaluated in § 3.1 and a comparison between the TDP model predictions and empirical measurements of a high-metallicity C IV absorber is presented in § 3.2.

#### 3.1. Model assumptions

Three key ingredients of time-dependent photoionization models are the underlying ionizing radiation, the initial temperature from which cooling occurs and the adopted abundance pattern. Reasonable choices for each ingredient are explored in the subsections here with § 3.1.1 discussing the impact of varying the adopted UVB, § 3.1.2 evaluating the effect of the chosen initial temperature, and § 3.1.3 examining the impact of using non-solar abundance patterns.

##### 3.1.1. UVB prescription

As discussed in § 2.1, there are several prescriptions available for the extragalactic UVB, which provides ionizing photons for the CGM. TDP models currently available in the public domain (see e.g., Oppenheimer & Schaye 2013; Gnat 2017)

adopt UVB models from HM05 and HM12. New UVB prescriptions from KS19 and FG20 show better agreement with Ly $\alpha$  forest observations, among other improvements. However, TDP models using KS19 and FG20 are not publicly available.

The right panel in Figure 4 shows the predicted TDP fractions for C IV, N V, and O VI for three different UVBs at  $z = 1$ , including HM12, KS19, and FG20. The predictions are obtained using the procedure described in § 2.2. The high-temperature ( $T > 10^5 \text{ K}$ ) peak comes from collisional ionization, while the low-temperature peak occurs because of photoionization. The fiducial choice of  $n_{\text{H}} = 0.001 \text{ cm}^{-3}$  and  $Z = Z_{\odot}$  for the density and metallicity are relevant to enriched C IV absorbers (§ 3.2). While ion fractions for C IV are robust against UVB choices, N V and O VI TDP fractions can differ by a factor of up to three at  $T \lesssim 10^5 \text{ K}$ . To facilitate a more focused discussion on the effect of TDP, FG20 is adopted as the fiducial UVB spectrum in the subsequent discussions.

##### 3.1.2. Initial temperature

A salient feature of TDP calculations is ion fractions' dependence on the gas's cooling history. This dependence is captured by solving the ionization and energy equations simultaneously. Therefore, the initial temperature from which the gas cools can affect TDP fractions at lower temperatures. Specifically, the gas is established to be in collisional ionization equilibrium (CIE) at the initial temperature  $T_0$  at the beginning of TDP calculations (§ 2.2). Because the CIE composition is temperature-dependent (see e.g., Gnat & Sternberg 2007), different initial compositions corresponding to unique choices of initial temperature may influence the subsequent time-dependent cooling.

Figure 5 depicts the TDP fractions for key species evaluated at  $T_{\text{eval}} = 3 \times 10^4 \text{ K}$  for different choices of initial temperature  $T_0$ . For reference, Gnat (2017) assume  $T_0 = 10^8 \text{ K}$  for their TDP calculations, while Oppenheimer & Schaye (2013) experiment with two temperatures,  $T_0 = 3 \times 10^6, 10^7 \text{ K}$ . It is found that the evaluated  $x_{\text{ion}}$ 's are robust for initial tempera-

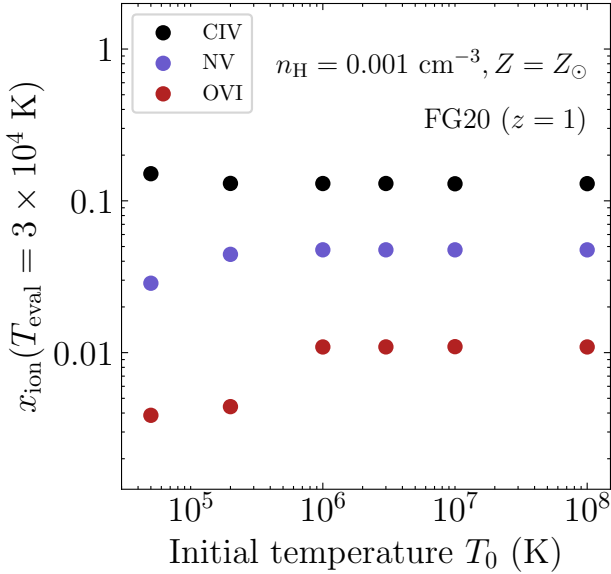


FIG. 5.—: Dependence of TDP ion fractions  $x_{\text{ion}}$  on the initial gas temperature  $T_0$  for the C IV, N V, and O VI ions. The resulting  $x_{\text{ion}}$  are evaluated at  $T_{\text{eval}} = 3 \times 10^4$  K. The FG20 UVB at  $z = 1$  is adopted, and the density and metallicity are assumed to be  $n_{\text{H}} = 0.001 \text{ cm}^{-3}$  and  $Z = Z_{\odot}$ .

tures of  $T_0 \geq 10^6$  K. However, the O VI fraction is depleted for  $T_0 \lesssim 10^6$  K by a factor of two, and the anticipated N V fraction decreases for  $T_0 \lesssim 10^5$  K by 25%, while the C IV fraction remains stable for the range of initial temperatures considered. The sensitivities of TDP ion fractions to different initial temperature can be understood by considering the CIE fractions of different ionization stages at these temperatures for different elements. For oxygen at initial temperatures cooler than  $T = 2 \times 10^5$  K, a substantial fraction remains at lower ionization stages under CIE, resulting in a lower initial  $\text{O}^{5+}$  abundance at the start of the cooling sequence and a still lower  $x_{\text{ion}}$  as the gas continues to cool.

The physical justification for exploring different initial temperatures is related to the possible dependence of the initial temperature with halo mass. A potential scenario is infalling clouds getting shock-heated to the halo’s virial temperature, giving rise to these intermediate- to high-ionization species. Galaxy hosts of these absorbers having a large range of halo masses (see e.g., Liang & Chen 2014; Bordoloi et al. 2014; Burchett et al. 2013; Zahedy et al. 2019; Qu et al. 2023), indicating a range of initial temperatures from which absorbers cool down under the infall scenario. Allowing flexibility in choosing the initial temperature for TDP calculations can thus help incorporate known galaxy host information in modeling these absorbers.

### 3.1.3. Elemental abundance pattern

Chemical elements are produced through different nucleosynthetic pathways. The  $\alpha$  elements (O, S, Mg, Si, Ne, etc.) primarily originate in core-collapse supernovae. However, carbon can have secondary contributions from AGB winds (see e.g., Kobayashi et al. 2020). For these reasons, both the  $\alpha$  elements and carbon can be expected to deviate from the solar expectation. The relative abundances, including  $[\text{C}/\alpha]$ ,  $[\text{N}/\alpha]$ , and  $[\text{Fe}/\alpha]$ , encapsulate the deviation of different elements from the solar pattern. The relative abundances of

elements set their contributions to gas cooling (see e.g., Gnat & Ferland 2012). Because  $x_{\text{ion}}$ ’s in PIE are evaluated independently of the gas cooling under a steady state assumption, relative abundances do not influence PIE fractions. However, ion fractions are coupled to gas cooling in TDP, meaning that relative abundances can affect TDP fractions.

Figure 6 shows the variation in TDP fractions and gas cooling using non-solar  $[\text{C}/\alpha]$  values. Despite carbon being an effective coolant, variations in  $[\text{C}/\alpha]$  have a small impact on the total gas cooling and TDP fractions. This is because at  $T \approx 4 \times 10^7$  K, which is the cooling peak of carbon, it only contributes to about 20% of the total cooling (assuming a solar pattern). The total cooling for  $[\text{C}/\alpha] = \pm 0.3$  is therefore respectively 20% higher and 10% lower compared to the original. The coupled  $x_{\text{ion}}$ ’s change by up to 40%. Nevertheless, the relative abundances must be accounted for when computing TDP column densities before comparing them with absorption line measurements between the ionization states of different elements.

### 3.2. Comparison with absorption line measurements

Paper I presented a sample of seven warm-hot C IV absorbers at  $z \sim 1$ , which were found to arise in relatively cool ( $T \lesssim 5 \times 10^4$  K), photoionized diffuse gas ( $n_{\text{H}} \approx 10^{-4} - 10^{-3} \text{ cm}^{-3}$ ). However, some systems show inferred gas metallicities exceeding solar values under a PIE assumption. As demonstrated in § 2.2, diffuse ionized gas in this regime can significantly depart from equilibrium due to rapid gas cooling. These high-metallicity systems also preferentially show a discrepancy in the inferred temperature between their best-fit ionization model and the observed thermal line width. To address these caveats of PIE models, a re-evaluation of the highest metallicity C IV absorption component from Paper I under the TDP framework is presented in this section.

This system at  $z_{\text{abs}} \approx 1.26$  consists of a single, narrow metal component of  $\log N_{\text{c}}(\text{CIV})/\text{cm}^{-2} = 12.78 \pm 0.03$  and  $b_{\text{c}}(\text{CIV}) = 6.0 \pm 0.7 \text{ km s}^{-1}$  identified using the high signal-to-noise Keck HIRES spectrum. Associated absorption in C III and O IV was identified in the *HST* STIS and COS spectrum, respectively, yielding a density estimate  $\log(n_{\text{H}}/\text{cm}^{-3}) \approx -3.3 \pm 0.2$  and relative abundance  $[\text{C}/\alpha] \approx 0.0$  under an equilibrium assumption. The metal-bearing H I component for this system was blended with adjacent H I components without associated metals. The profile decomposition for H I was performed collectively using transitions  $\text{Ly}\alpha$ ,  $\text{Ly}\beta$ , and  $\text{Ly}\gamma$  available in the *HST* STIS spectrum. This yielded a relatively small H I column density of  $\log N_{\text{c}}(\text{HI})/\text{cm}^{-2} = 12.9 \pm 0.1$  associated with the detected metals. The observed relative ion to hydrogen ratios lead to a high inferred metallicity of  $[\alpha/\text{H}] = +0.6^{+0.2}_{-0.1}$ , approximately  $4\times$  solar with a solar metallicity ruled out at a  $6\text{-}\sigma$  level of significance and no luminous galaxies found in the vicinity of the absorber.

The posterior distribution for the gas density and metallicity were used to obtain the predicted ionization model temperatures,  $T_{\text{PIE}}$ . Owing to the high gas metallicity, ionization models prefer a very cool gas with median equilibrium temperature  $T_{\text{PIE}} \approx 5000$  K, and a stringent  $3\text{-}\sigma$  upper limit of  $13000$  K (see Table 1). The ionization model temperature is inconsistent with the thermal temperature  $T \approx 23440$  K obtained by comparing the H I line width,  $b_{\text{c}}(\text{HI}) = 20 \pm 2 \text{ km s}^{-1}$ , with the metal absorption. The coincidence of this discrepancy with the high inferred metallicity of this component motivates

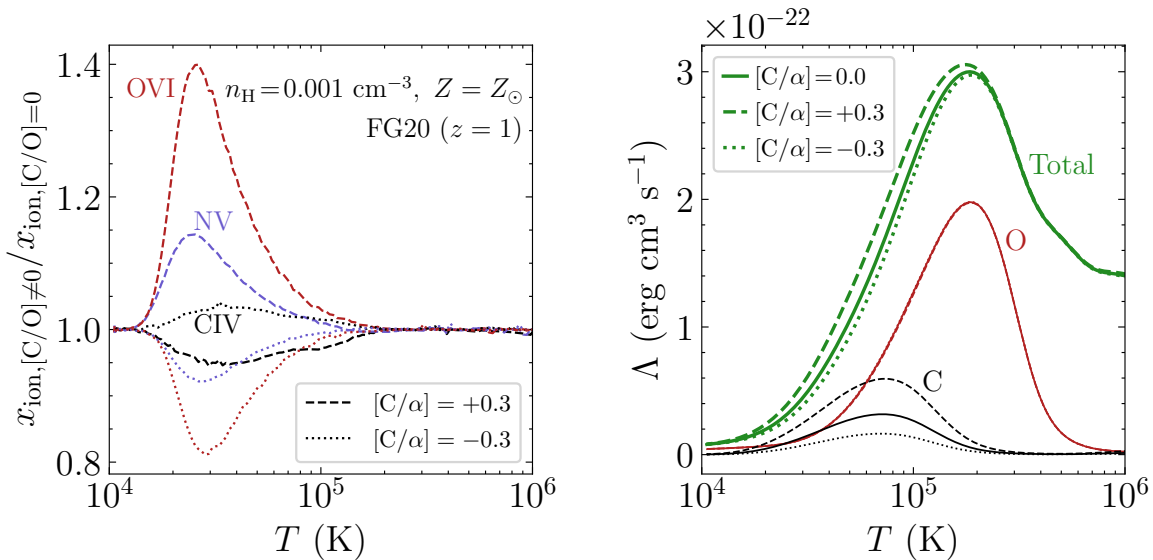


FIG. 6.— Impact of non-solar  $[C/\alpha]$  relative abundances on the predicted ion ratios. The *left* panel depicts the ratio of TDP fractions evaluated assuming non-solar  $[C/O]$  ratios relative to the standard solar values. Examples with super- and sub-solar  $[C/\alpha]$  are shown with different line styles. The FG20 UVB at  $z = 1$  is adopted, along with a density of  $n_{\text{H}} = 0.001 \text{ cm}^{-3}$  and metallicity of  $Z = Z_{\odot}$ . The *right* panel depicts TDP cooling losses assuming a non-solar  $[C/\alpha]$  ratio. Individual contributions from carbon and oxygen are depicted in different colors. The total includes contribution from nitrogen,  $\alpha$ -elements like neon and sulfur, as well as light elements like hydrogen and helium.

TABLE 1: Inferred physical properties for component c3 of the  $z_{\text{abs}} = 1.25937$  absorber presented in Paper I.

Property	TDP <sup>a</sup>	PIE
$\log(n_{\text{H}}/\text{cm}^{-3})$	$-3.2 \pm 0.1$	$-3.3 \pm 0.2$
$T$ (K)	$2.3 \times 10^4$ <sup>a</sup>	$< 1.3 \times 10^4$ <sup>b</sup>
$[\alpha/\text{H}]$	$0.4 \pm 0.2$	$0.6^{+0.2}_{-0.1}$
$[C/\alpha]$	$0.25 \pm 0.08$	$0.00 \pm 0.09$
$[\text{N}/\alpha]$	$< 0.8$	$< 0.6$
$\log(l/\text{kpc})$	$-1.8^{+0.3}_{-0.2}$	$-1.9 \pm 0.3$

<sup>a</sup> Line-width determined temperature.

<sup>b</sup>  $3\text{-}\sigma$  upper limit on the PIE temperature. The best-fit PIE models suggest that the gas cools to a median temperature of  $\approx 5000$  K

its reassessment under the TDP framework discussed below.

Unlike PIE, thermal equilibrium is not assumed in TDP. A comparison between predicted and observed ionic column densities of this component is performed for a gas temperature of  $T_{\text{TDP}} = 23440$  K as determined from comparing absorption line widths of different elements. The model predictions are calculated over a grid of gas parameters. The conversion from TDP fractions  $x_{\text{ion}}$  to column densities is achieved by assuming  $\log(N_{\text{H}}/\text{cm}^{-2}) = 12.9$  (see Equation (3) from Paper I). A posterior distribution is constructed for gas parameters using MCMC sampling utilities provided by the emcee library in Python (Foreman-Mackey et al. 2013). The likelihood definition used for this evaluation is taken from Paper I, wherein sensitive upper limits on column density for non-detections are accounted for in addition to measurements. The best-fit values and associated uncertainties for various gas properties are summarized in Table 1. Estimates for both the TDP and PIE frameworks are listed in the table to facilitate direct comparisons.

The best-fit model parameters summarized in Table 1 confirm that relaxing the equilibrium condition reduces the inferred gas metallicity. Although the best-fit gas metallicity

remains high at  $[\alpha/\text{H}] = +0.4$ , solar metallicity cannot be ruled out at a significant level. In addition, a modest non-solar  $C/\alpha$  elemental abundance pattern of  $[C/\alpha] = 0.25$  is needed to explain the observed abundances of carbon ions.

To further visualize the allowed parameter range, Figure 7 illustrates how the observed ionic column density ratios depend on the gas temperature. The  $x$ -axis in all three panels is chosen to be the C IV/C III ratio, which has the benefit of being independent of the underlying abundance pattern despite a large uncertainty in  $N(\text{CIII})$ . The observed column density ratios and associated uncertainties are respectively marked by a star symbol and a dashed ellipse in each panel. The model curves track the changes in the ionization state of the gas as it cools. Model predictions are shown for the best-fit gas density of  $\log(n_{\text{H}}/\text{cm}^{-3}) = -3.2$  and the  $1\text{-}\sigma$  lower-bound of the best-fit metallicity,  $[\alpha/\text{H}] = +0.2$ . Column density ratios for the allowed temperature range (68% interval around the best-fit line-profile temperature) are indicated in red. The two left panels of Figure 7 demonstrate that with a solar abundance pattern (dotted curve), the best-fit TDP model with only slightly enhanced gas metallicity  $[\alpha/\text{H}] = 0.2$  can already reproduce the observed C IV/O IV and O IV/H I ratios to within the measurement uncertainties, while it underproduces the observed C IV/H I ratio displayed in the right panel. To mitigate the discrepancy between observed and model C IV/H I ratios would require increasing the relative carbon abundance to  $[C/\alpha] \approx +0.3$  (solid curve in all panels). A still higher  $[C/\alpha]$  value would increase the tension between the observed and predicted C IV/O IV displayed in the left panel.

#### 4. SUMMARY AND DISCUSSION

This paper presents an updated framework for computing time-dependent photoionization models, integrating the latest UVB prescriptions and atomic data. Specifically, the study focuses on high-metallicity gas, in which rapid cooling results

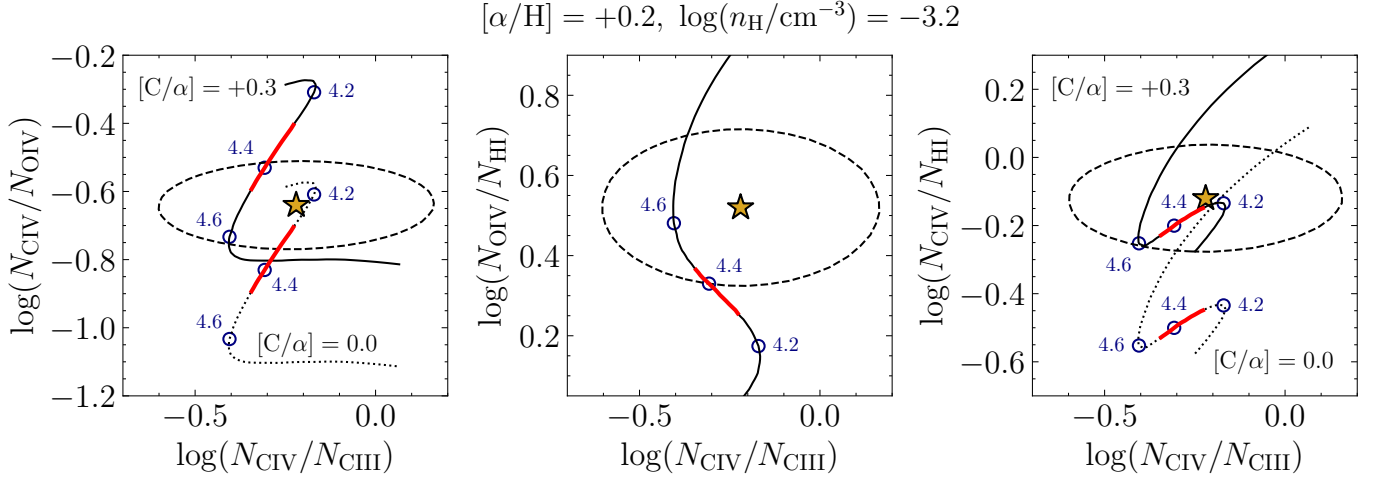


FIG. 7.—: Re-evaluation of a C IV absorber at  $z \approx 1.26$  from Kumar et al. (2024) under TDP and non-solar abundance pattern. From left to right, the panels show respectively observed and predicted C IV/O IV, O IV/H I, and C IV/H I versus the C IV/C III ratio. The observed values are marked by a star symbol, with the corresponding 68% error ellipse drawn with a dashed line. TDP model predictions in each panel are shown for a fiducial gas metallicity  $[\alpha/H] = +0.2$  and density  $\log(n_{\text{H}}/\text{cm}^{-3}) = -3.2$  at different temperatures with the corresponding  $\log T/\text{K}$  marked in blue color. The  $1-\sigma$  interval in temperature inferred from line width measurements is highlighted in thick red segments. For ratios C IV/O IV and C IV/H I, the model predictions also depend on the relative carbon abundance. Therefore, two sets of model predictions based on  $[C/\alpha] = 0.0$  and  $+0.3$  are shown in dotted and solid curves, respectively.

in a recombination lag and enhances the abundances of higher ionization states. The findings demonstrate that accounting for the possibility of highly enriched CGM absorbers being out of equilibrium helps resolve the discrepancy between the thermal temperatures derived from absorption line profiles and the photoionization temperatures predicted by best-fit equilibrium ionization models. In addition, it minimizes the necessity of invoking uncharacteristically high super-solar gas metallicities to explain the observed ion abundances. Under TDP, solar metallicity cannot be ruled out with more than  $2-\sigma$  significance, while a modest non-solar  $[C/\alpha] = 0.25 \pm 0.08$  is needed to explain the observed relative ion abundances. Extensive studies have also investigated the impact of different model assumptions involving the choice of a particular UVB prescription, the initial temperature, and the adopted elemental abundance pattern. The lessons learned from this exercise are summarized here.

First, the expected abundances of common ionization species traced by C IV, N V, and O VI are sensitive to the slope and amplitude of the adopted UVB (see Figure 4 and § 3.1.1). This sensitivity arises because higher radiation intensities result in increased abundances of ions with ionization potentials matching the photon energies at these high frequencies (see e.g., Figure 1). Notably, this effect persists regardless of whether the gas is in equilibrium.

Secondly, while the initial temperature  $T_0$  is expected to influence the subsequent production of intermediate- to low-ionization species under a rapidly cooling process, only  $\text{O}^{5+}$  ions exhibit appreciable changes (by a factor of  $\geq 2$ ) in the predicted TDP fractions when  $T_0 = 10^5\text{--}10^6$  K was adopted. No detectable differences are found for  $\text{C}^{3+}$  or  $\text{N}^{4+}$  with  $T_0 > 10^5$  K (see Figure 5 and § 3.1.2). The sensitivity of the predicted  $\text{O}^{5+}$  abundances under TDP can be explained by the expectation that under equilibrium conditions the abundances of these ions peak at a temperature higher than  $T_0$  and, therefore, a lower initial abundance is expected at  $T_0$ . Conversely,  $\text{C}^{3+}$  or

$\text{N}^{4+}$  have peak temperatures comparable to or lower than the initial temperatures considered, rendering their resulting TDP fractions insensitive to the adopted  $T_0$ .

Finally, as illustrated in Figure 6, cooling at  $T > 10^5$  K is driven by metal ions. The expected TDP ion fractions should naturally depend on the underlying elemental abundance pattern. Indeed, changing the relative carbon to  $\alpha$ -element abundance pattern can lead to different expected ion fractions by 5-40% at  $T < 10^5$  K under the TDP scenario, with the largest anticipated differences for O VI (§ 3.1.3). The relatively modest effect under a non-solar  $[C/\alpha]$  pattern arises because carbon only contributes to  $\approx 20\%$  of the total cooling at its peak,  $T \approx 4 \times 10^7$  K assuming a solar pattern.

However, caveats remain. A direct consequence of non-equilibrium conditions is that the gas is in a transient state as it continues to cool, posing challenges in constructing a steady-state model for characterizing the origin of these metal-line absorbers as a whole. Alternatively, the temperature discrepancy under PIE can be addressed by introducing an unknown heating source to elevate the heating rate (see Figure 2) and maintain the temperature at the value suggested by thermal broadening during photoionization calculations (e.g., Hussain et al. 2015; Pachat et al. 2017; see also Qu et al. 2023). The challenge in this scenario is maintaining the required heating level without significantly modifying the relative ion abundances. While turbulence may be a suitable heating agent as it does not generate ionizing photons, the small non-thermal broadening observed in the case study (§ 3.2) with  $b_{\text{NT}} < 6$  km s $^{-1}$  (a  $3-\sigma$  limit, see Appendix A5 in Paper I) does not support this scenario.

Irrespective of the challenges associated with TDP and the warm PIE models, current observations do not provide the precision needed to discriminate between the two scenarios. Because recombination lags are expected to result in an overabundance of higher ionization species from non-equilibrium cooling, producing characteristically different abundances of

successive ionization stages compared to the equilibrium scenario, improved measurements of multiple ionization stages with reduced uncertainties help strengthen the distinguishing power between PIE and TDP solutions statistically. Extending the TDP analyses to a larger sample of super-solar absorption components with high signal-to-noise data for successive ionization stages is needed to better quantify the fraction of metal absorbers originating in rapid cooling gas.

## ACKNOWLEDGEMENTS

The authors thank Zhijie Qu, Harley Katz, and Gwen Rudie for helpful discussions throughout this work. S.K. thanks Mu-Chen Hsieh and Rohan Venkat for testing the user-friendliness of open source CLOUDY scripts and Python routines used to create model grids used in this work. H.-W.C. and S.K. acknowledge partial support from HST-GO-17517.01A and NASA ADAP 80NSSC23K0479 grants.

## REFERENCES

- Bergeron J., Stasińska G., 1986, *A&A*, **169**, 1  
 Bordoloi R., et al., 2014, *ApJ*, **796**, 136  
 Borthakur S., Heckman T., Strickland D., Wild V., Schiminovich D., 2013, *ApJ*, **768**, 18  
 Burchett J. N., Tripp T. M., Werk J. K., Howk J. C., Prochaska J. X., Ford A. B., Davé R., 2013, *ApJ*, **779**, L17  
 Burchett J. N., et al., 2015, *ApJ*, **815**, 91  
 Burchett J. N., et al., 2016, *ApJ*, **832**, 124  
 Burchett J. N., et al., 2019, *ApJ*, **877**, L20  
 Chatzikos M., et al., 2023, *Rev. Mexicana Astron. Astrofis.*, **59**, 327  
 Chen H.-W., Prochaska J. X., 2000, *ApJ*, **543**, L9  
 Chen H.-W., Lanzetta K. M., Webb J. K., 2001, *ApJ*, **556**, 158  
 Chen H.-W., Helsby J. E., Gauthier J.-R., Shectman S. A., Thompson I. B., Tinker J. L., 2010, *ApJ*, **714**, 1521  
 Chen H.-W., Johnson S. D., Zahedy F. S., Rauch M., Mulchaey J. S., 2017, *ApJ*, **842**, L19  
 Cooper T. J., et al., 2021, *MNRAS*, **508**, 4359  
 Crighton N. H. M., Hennawi J. F., Simcoe R. A., Cooksey K. L., Murphy M. T., Fumagalli M., Prochaska J. X., Shanks T., 2015, *MNRAS*, **446**, 18  
 Faucher-Giguère C.-A., 2020, *MNRAS*, **493**, 1614  
 Ferland G. J., et al., 2017, *Rev. Mexicana Astron. Astrofis.*, **53**, 385  
 Foreman-Mackey D., Hogg D. W., Lang D., Goodman J., 2013, *PASP*, **125**, 306  
 Gnat O., 2017, *ApJS*, **228**, 11  
 Gnat O., Ferland G. J., 2012, *ApJS*, **199**, 20  
 Gnat O., Sternberg A., 2007, *ApJS*, **168**, 213  
 Haardt F., Madau P., 2001, in Neumann D. M., Tran J. T. V., eds, *Clusters of Galaxies and the High Redshift Universe Observed in X-rays*. p. 64 ([arXiv:astro-ph/0106018](https://arxiv.org/abs/astro-ph/0106018)), doi:10.48550/arXiv.astro-ph/0106018  
 Haardt F., Madau P., 2012, *ApJ*, **746**, 125  
 Haislmaier K. J., Tripp T. M., Katz N., Prochaska J. X., Burchett J. N., O’Meara J. M., Werk J. K., 2021, *MNRAS*, **502**, 4993  
 Huang Y.-H., Chen H.-W., Johnson S. D., Weiner B. J., 2016, *MNRAS*, **455**, 1713  
 Huang Y.-H., Chen H.-W., Shectman S. A., Johnson S. D., Zahedy F. S., Helsby J. E., Gauthier J.-R., Thompson I. B., 2021, *MNRAS*, **502**, 4743  
 Hussain T., Muzahid S., Narayanan A., Srianand R., Wakker B. P., Charlton J. C., Pathak A., 2015, *MNRAS*, **446**, 2444  
 Keeney B. A., Stocke J. T., Rosenberg J. L., Danforth C. W., Ryan-Weber E. V., Shull J. M., Savage B. D., Green J. C., 2013, *ApJ*, **765**, 27  
 Keeney B. A., et al., 2017, *ApJS*, **230**, 6  
 Khaire V., Srianand R., 2019, *MNRAS*, **484**, 4174  
 Kobayashi C., Karakas A. I., Lugaro M., 2020, *ApJ*, **900**, 179  
 Kumar S., Chen H.-W., Qu Z., Chen M. C., Zahedy F. S., Johnson S. D., Muzahid S., Cantalupo S., 2024, *The Open Journal of Astrophysics*, 7  
 Lehner N., et al., 2022, *ApJ*, **936**, 156  
 Liang C. J., Chen H.-W., 2014, *MNRAS*, **445**, 2061  
 Meiring J. D., Tripp T. M., Werk J. K., Howk J. C., Jenkins E. B., Prochaska J. X., Lehner N., Sembach K. R., 2013, *ApJ*, **767**, 49  
 Nevalainen J., Wakker B., Kaastra J., Bonamente M., Snowden S., Paerels F., de Vries C., 2017, *A&A*, **605**, A47  
 Oppenheimer B. D., Schaye J., 2013, *MNRAS*, **434**, 1043  
 Pachat S., Narayanan A., Khaire V., Savage B. D., Muzahid S., Wakker B. P., 2017, *MNRAS*, **471**, 792  
 Peeples M. S., Werk J. K., Tumlinson J., Oppenheimer B. D., Prochaska J. X., Katz N., Weinberg D. H., 2014, *ApJ*, **786**, 54  
 Qu Z., et al., 2022, *MNRAS*, **516**, 4882  
 Qu Z., et al., 2023, *MNRAS*, **524**, 512  
 Qu Z., et al., 2024, *ApJ*, **968**, 8  
 Rauch M., Sargent W. L. W., Womble D. S., Barlow T. A., 1996, *ApJ*, **467**, L5  
 Rauch M., Haehnelt M. G., Steinmetz M., 1997, *ApJ*, **481**, 601  
 Rosenwasser B., Muzahid S., Charlton J. C., Kacprzak G. G., Wakker B. P., Churchill C. W., 2018, *MNRAS*, **476**, 2258  
 Rudie G. C., Steidel C. C., Pettini M., Trainor R. F., Strom A. L., Hummels C. B., Reddy N. A., Shapley A. E., 2019, *ApJ*, **885**, 61  
 Sameer et al., 2021, *MNRAS*, **501**, 2112  
 Sameer et al., 2024, *MNRAS*, **530**, 3827  
 Sankar S., Narayanan A., Savage B. D., Khaire V., Rosenwasser B. E., Charlton J., Wakker B. P., 2020, *MNRAS*, **498**, 4864  
 Tripp T. M., et al., 2011, *Science*, **334**, 952  
 Werk J. K., et al., 2014, *ApJ*, **792**, 8  
 Wiersma R. P. C., Schaye J., Smith B. D., 2009, *MNRAS*, **393**, 99  
 Zahedy F. S., Chen H.-W., Johnson S. D., Pierce R. M., Rauch M., Huang Y.-H., Weiner B. J., Gauthier J.-R., 2019, *MNRAS*, **484**, 2257  
 Zahedy F. S., et al., 2021, *MNRAS*, **506**, 877

This paper was built using the Open Journal of Astrophysics  $\LaTeX$  template. The OJA is a journal which provides fast and easy peer review for new papers in the astro-ph section of

the arXiv, making the reviewing process simpler for authors and referees alike. Learn more at <http://astro.theoj.org>.